Thermal pressurization induced the frequency-dependent rupture during the 2019 M_w8.0 Peru intermediate-depth earthquake

Heng Luo[1], Hongyu Zeng[2], Qibin Shi[2], Teng Wang[3]*, Mingsheng Liao[1]*, Jianya Gong[1,4], Jiashun Hu[5] and Shengji Wei[2,6]*

[1] State Key Laboratory of Information Engineering in Surveying, Mapping, and Remote Sensing, Wuhan University, China

[2] Asian School of the Environment, Nanyang Technological University, Singapore

[3] Earth and Space Science Department, Peking University, China

[4]School of Remote Sensing and Information Engineering, Wuhan University, China

[5]Seismological Laboratory, California Institute of Technology, USA

[6]Earth Observatory of Singapore, Nanyang Technological University, Singapore

Corresponding authors:

Teng Wang (wang.teng@pku.edu.cn)

Mingsheng Liao (liao@whu.edu.cn)

Shengji Wei (shjwei@ntu.edu.sg)

Heng Luo and Hongyu Zeng made equal contributions to this work.

Key Points:

- The rupture process of the 2019 M_w Peru earthquake occurred at 122km depth is imaged by teleseismic and InSAR observations.
- The largest asperity radiated much weaker high-frequency seismic waves compared to other smaller asperities.
- Thermal pressurization of pore free water rather than thermal runaway likely explains the distinct frequency-dependent rupture.

Abstract

The rupture process of earthquakes at intermediate-depth (~70-300 km) have been rarely illuminated by a joint analysis of geodetic and seismic observations, hindering our understanding on their dynamic rupture mechanisms. Here we present detailed rupture process of the 2019 M_w8.0 Peru earthquake at the depth of 122 km with a holistic approach reconciling InSAR and broadband seismological waveform data. The joint inversion of InSAR observations and teleseismic body waves results in a finite rupture model that extends ~200 km along strike, with unilateral rupture towards north that lasted for ~60 s. There are four major asperities in the finite fault model which are well corresponding to position and timing of the sources in back-projection (BP) and multiple points source (MPS) results. The largest asperity, which occurred ~40 s after the

rupture initiation, was featured with longer and smoother risetime, and radiated much weaker high-frequency seismic waves compared to other smaller asperities. This distinct frequency-dependent rupture requires a strong dynamic weakening mechanism, likely thermal pressurization of pore free water rather than thermal runaway. Our frequency content analysis could be generalized to study other earthquakes including those deeper than 300 km.

1 Introduction

The mechanism of the intermediate-depth (~70-300 km) earthquakes that occur within the subducted oceanic lithosphere is one of the most puzzling issues in seismology as brittle dislocation should be forbidden in such high confined pressure. The explanation for the mechanism has over the years been sought using various approaches, for example, stress drop analysis (e.g. (Germán A. Prieto *et al.*, 2013), source time functions (e.g. Houston *et al.*, 1998), seismicity and aftershock distributions (e.g. Germán A Prieto *et al.*, 2012), finite rupture process analysis (e.g. Melgar *et al.*, 2018), rock experiments (e.g. Jung *et al.*, 2004; Okazaki and Hirth, 2016), geological and mineral analysis (e.g. Brudzinski *et al.*, 2007; John and Schenk, 2006; Kirby *et al.*, 1996). The studies have settled on two most possible hypotheses: dehydration embrittlement (e.g. Green and Houston, 1995; Hacker *et al.*, 2003) and thermal runaway (e.g. John *et al.*, 2009; Kelemen and Hirth, 2007). According to the dehydration embrittlement hypothesis, hydrous minerals in the subducted oceanic lithosphere, principally serpentine, release water into the pore space in the surrounding rocks at intermediate depths. This process increases the pore fluid pressure, facilitating frictional sliding, and consequently triggering earthquakes. Under this mechanism, the thermal pressurization of pore fluid, that is fault friction causes the fluids within the fault shear zone to heat up and expand, could play an important role during the dynamic rupture process. Although thermal pressurization has been proposed to explain rupture and stress evolution of shallow earthquakes (e.g. Sibson, 1973; Rice, 2006), it has not yet been reported in intermediate-depth earthquake observations. In comparison, according to the thermal runaway hypothesis, positive feedback between shear heating and temperature-dependent rock softening possibly results in partial rock melting which triggers earthquakes. Both hypotheses have supports from laboratory experiments and natural earthquakes, making the dynamic rupture mechanism of intermediate-depth earthquake still under debate.

One of the most commonly adopted ways to understanding the mechanisms of earthquakes is to analyse earthquake ruptures using seismic observations, as such approach can directly constrain earthquake source parameters. This approach includes finite fault modelling (FFM) (e.g. Wei *et al.*, 2015; Wei *et al.*, 2013), multiple point source inversions (MPS) (e.g. Chen *et al.*, 2014; Shi *et al.*, 2018), and the more recently developed back-projection (BP) methods (e.g. Zeng *et al.*, 2020; Meng *et al.*, 2012). Geodetic measurements, on the other hand, are complementary with seismic data in determining the source location and fault geometry when applying joint FFM inversions (e.g. Avouac

et al., 2015; Wang *et al.*, 2018; Wei *et al.*, 2011). However, to date, to the best of our knowledge, only three intermediate-depth events: the Kash M_w7.7 earthquake (Barnhart *et al.*, 2014), the Tarapaca M_w7.8 earthquake (Peyrat *et al.*, 2006), and the Tehuantepec M_w8.2 earthquake (Melgar *et al.*, 2018), have been studied by combining geodetic and seismological inversions. None of the studies has applied all these methods holistically (i.e., joint inversion of seismological and geodetic data together with BP and MPS) to cover broader range of source spectrum, although such a holistic approach has been clearly demonstrated to reveal greater rupture details in studying shallow earthquakes (e.g. Avouac *et al.*, 2015). The lacuna of holistic studies is not surprising, given that large intermediate-depth events are rarer inland, and the magnitude of the earthquakes have to be sufficiently large (e.g. $>$ M_w7.5) to be recorded by geodetic data. The May 26, 2019 M_w8.0 Peru earthquake was such a rare event, and was additionally well captured in satellite images, providing a unique opportunity to jointly analyse the seismological and geodetic observations to reveal its rupture process.

The 2019 M_w8.0 Peru earthquake occurred at an intermediate depth of 122 km (National Earthquake Information Centre, NEIC) within the Nazca plate, which is subducting beneath the South American plate at a velocity of ~58 mm/yr (Kreemer *et al.*, 2014) (Figure 1a). Global Centroid Moment Tensor (GCMT) reported a pure normal faulting solution on a moderately-dipping (~50°) fault oriented nearly N-S (Ekstrom *et al.*, 2012). Based on the Slab1.0 model (Hayes *et al.*, 2012), the earthquake was located near the eastern edge of the flat portion of the Nazca plate (Figure 1a). This massive quake generated large-scale surface deformation, mostly inland, that was clearly captured by Sentinel-1 Synthetic Aperture Radar (SAR) interferograms (Figure 1b). The accurate geodetic measurements, along with broadband seismological observations, allow us to well constrain the ground-truth location of the earthquake, fault geometry and rupture process of the earthquake, making it an unprecedented case to further understand the mechanism of intermediate-depth earthquake.

The rupture process of the 2019 M_w8.0 Peru earthquake was already reported by a few studies. Ye et al. (2020) used finite fault inversion of teleseismic body waves to reveal a rupture speed of ~3.0 km/s and pointed out the anomalously low aftershock productivity. Liu and Yao (2020) studied the earthquake rupture with teleseismic finite fault inversion and back-projection of high frequency array waveforms. They found that the high frequency and lower frequency sources are highly consistent in strength, location and timing. More recently, Hu et al. (2021) also adopted back-projection and finite fault inversion with flexible fault geometry to study the rupture process of the earthquake. Their result shows a much smoother slip model than the other studies. They explained this discrepancy with higher degrees of freedom and stronger smoothing parameter in their inversion. In this study, we incorporate InSAR observations along with a set of seismological approaches, including BP, MPS inversion, FFM inversion and high frequency envelope analysis, to cover a wider range of source spectrum that has not yet been fully investigated.

Here, we first present our BP result from the North America array, followed by our InSAR measurements and geodetic-only slip inversion. The rupture directivity derived from BP and the geodetic slip model allow us to discriminate the fault geometry from two nodal planes. Then we present the FFM result derived from the joint inversion of teleseismic body waves and InSAR measurements, followed by verification from MPS analysis. We find that the discrepancies between the BP and FFM results are supported by high frequency envelope analysis and can be well explained by the risetime duration contrast between the largest and smaller asperities. Lastly, we discuss the implications of this finding for the thermal pressurization mechanism of intermediate-depth earthquakes.

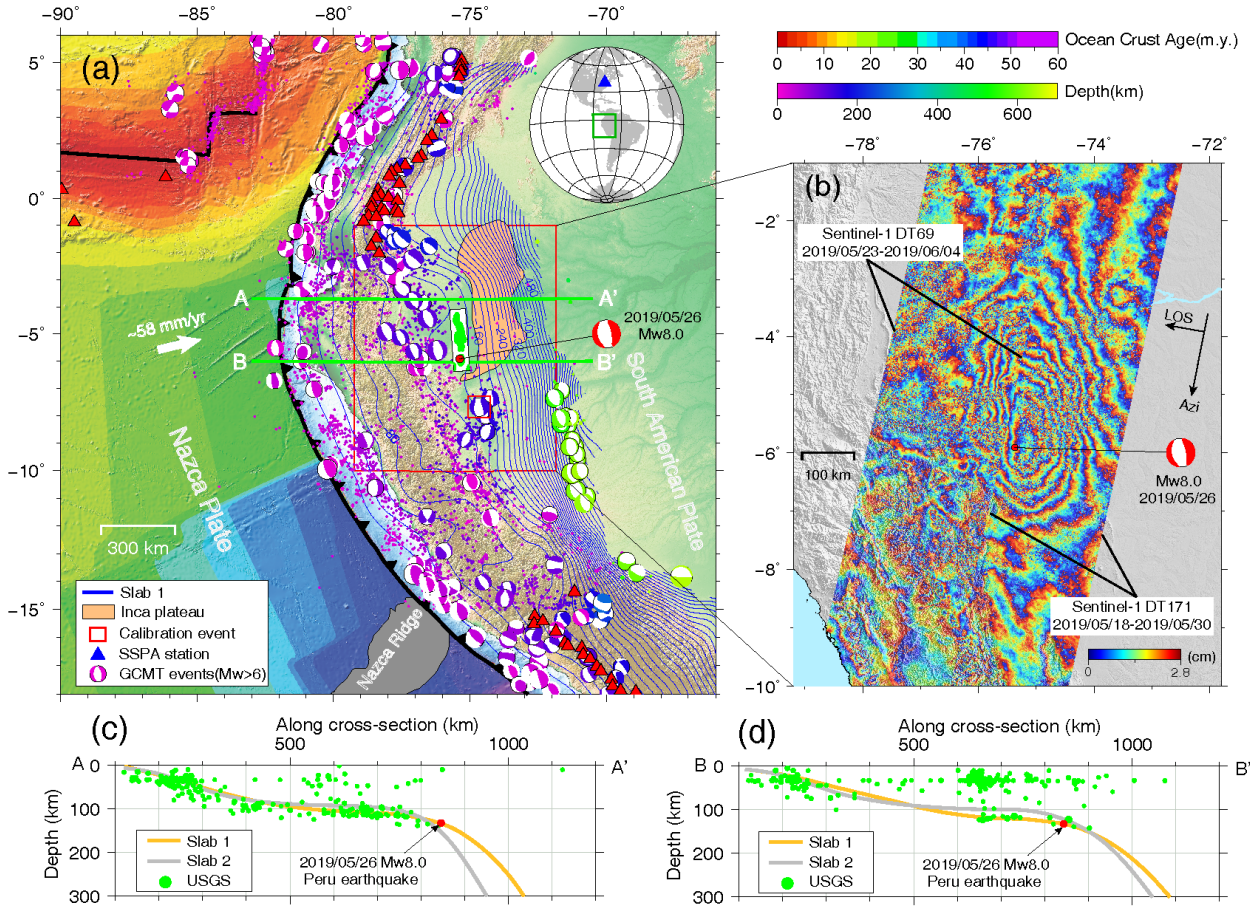

Figure 1. Overview of the study region and coseismic interferograms produced by Sentinel-1 SAR images. (a) The map shows the subduction of the Nazca plate beneath the northern part of the South American plate. The sea floor is coloured by its age (Muller *et al.*, 2008), and the blue contours show the depth of the interface of Slab1.0 model (Hayes *et al.*, 2012). The blue triangle in inset

represents the SSPA seismological station of the North American array, whose seismograms are analysed later. The plate boundaries are shown as bold black lines. The beach balls represent moment tensor solutions for M_w>6 events from GCMT project (Ekstrom *et al.*, 2012), and the coloured dots represent M>4.5 events from the U.S. Geological Survey (USGS), both shaded by their depths. The GCMT solution of the Peru M_w8.0 event is indicated by the red beach ball connecting to the USGS-determined epicentre (red dot). The event used in MPS path calibration is highlighted by a small red square. The red triangles represent volcanos (Global Volcanism Program, 2013). Note the lack of volcanos between 3° S and 15° S. The black frame indicates the area shown in (b). (b) Coseismic interferograms by Sentinel-1 images in track DT69 and DT171. Each fringe represents 2.8 cm of surface deformation along the radar's line-of-sight direction, and phase increasing indicates that the motion is away from the satellites. (c and d) The panels show the depth profiles along A-A' and B-B' in (a), along with seismicity (green dots), Slab1 (Hayes *et al.*, 2012) and Slab2 (Hayes *et al.*, 2018) models (orange and gray lines, respectively).

2. Data, method and results

2.1 Back-projection

2.1.1 Data and method

We adopt the MUSIC back-projection method (Zeng *et al.*, 2019; Meng *et al.*, 2012) to image the kinematic rupture process of the Peru earthquake by using the North America array P-wave data (Figure S1a). This technique back-propagates the waveforms to the source region to trace the sources of the coherent high-frequency energy in frequency-domain. For the beginning part of the rupture, the theoretical travel-time that calculated from 1D global velocity models (e.g., PREM) is usually calibrated by aligning the first several seconds of observed P waves (Ishii *et al.*, 2005). However, due to the complicated 3D source-side velocity structure, this calibration may not work well for rupture area that is far away from the epicentre. Additional calibration should be applied to correct this travel time error. We select three smaller intermediate-depth events (2012/11/28, Mw5.6; 2017/01/02, Mw5.9 and 2019/05/29, Mb 4.8) to the north of the mainshock epicentre and conduct BP using the travel time calibration from the mainshock hypocentre. The results show that high frequency sources are offset from the epicentres by ~20 km (Figure S1b-d), suggesting that additional calibrations should be and could be derived from events closer to the later part of the mainshock rupture. Here, we apply an interpolation algorithm to the travel time corrections from the mainshock and the three smaller events to calibrate the source-side 3D velocity structure (see supplement material for more details, also see Zeng and Wei (2019)). These calibrations are used to update the travel-time table in the back-projection of teleseismic P waves recorded at the North American array (Figure S1a) to image rupture process of the mainshock.

2.1.2 Results

With path calibration from three smaller earthquakes (Figure S1 and supple-

ment text), the mainshock BP result from the North American array is displayed in Figure 2 as the spatial and temporal evolution of the High Frequency (HF) radiators, which can be clearly clustered into four groups (H1-H4 in Figure 2). We can observe a clear lineation of these groups that shows the rupture lasted ~60 s and propagated unilaterally northward ~170 km. Beyond the initial 60 s, the BP signals are much weaker, probably the artefacts of depth phases (Figure S1). This lineation is highly consistent with the strikes of the nodal planes in the focal mechanism (353° and 166°). The smooth linear relationship between the timing and location of these HF clusters reveals a near-constant rupture speed of ~3.0 km/s. Strong HF energy is radiated by ruptures near the epicentre (H1), 40 - 80 km (H2) and 140 - 160 km away (H4) from the epicentre (Figure 2). The power of high frequency energy of the BP result is shown in Figure 3a (red lines), where the highlighted peaks (H1-H4) are corresponding to the map view of the clusters. Note the much weaker amplitude of H3, which will be interpreted and discussed later.

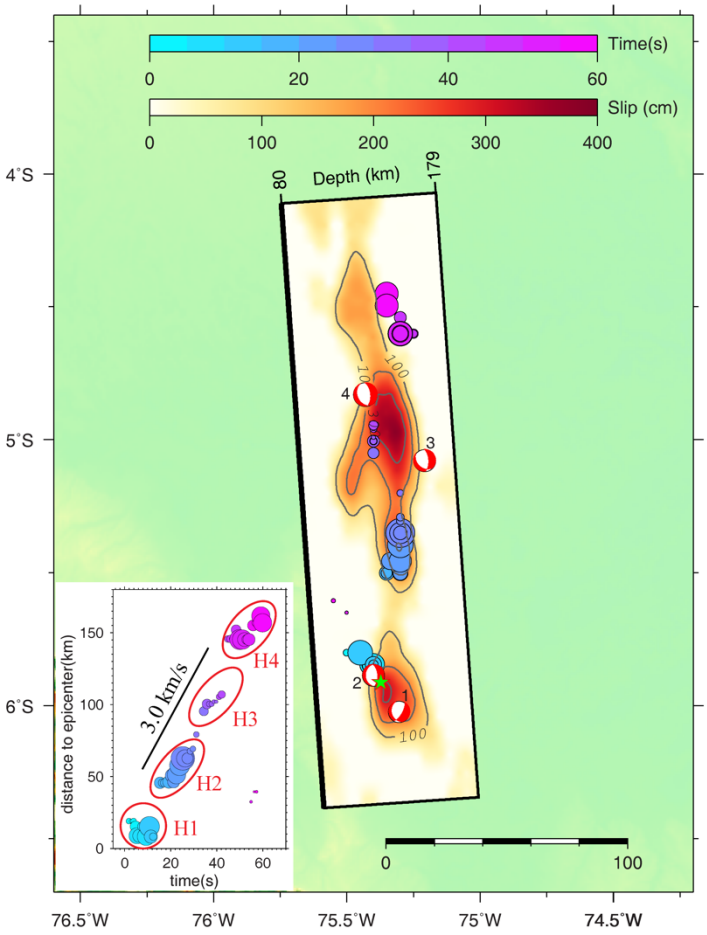

Figure 2. Map view of the preferred rupture kinematic models. The fault slips are derived from the joint FFM inversion. The BP's HF radiators are indicated by the colored circles, with their size proportional to the amplitude of the BP power. The red beachballs (1-4) represent the four major subevents derived from MPS inversion. The inset shows the spatial temporal relationship of the BP result in four clusters numbered by their distance from the epicentre (H1-H4), with an estimated rupture speed of 3.0 km/s.

2.2 InSAR data processing and static slip model inversion

2.2.1 Data and method

To obtain the geodetic observations for the earthquake, We collect multi-frame Sentinel-1 SAR images from six tracks to ensure the complete coverage of the deforming area of the 2019 Peru earthquake as possible (Figure S2). These images are processed using the burst-based processing chain implemented in the Sentinel-1 Interferometry Processor (http://sarimggeodesy.github.io/software) (Jiang *et al.*, 2017). The Digital Elevation Model (DEM) from Shuttle Radar Topography Mission (SRTM) is used for co-registration and for topography phase removal. The interferogram of each burst is multi-looked at first and then mosaicked into one ~250-kilometer wide interferogram with multi frames along the same track. The phase discontinuity between adjacent bursts is estimated from burst-overlap interferometry and satellite parameters, and is corrected before mosaicking (Yague-Martinez *et al.*, 2016). Because smooth coseismic deformation signal is expected, large multi-looking factors are applied as 10 pixels in azimuth and 40 pixels in range. Then the mosaicked interferograms are filtered using the Goldstein method to further improve the signal-to-noise ratio (SNR) (Goldstein and Werner, 1998). All interferograms are unwrapped by the Statistical-cost, Network-flow Algorithm for Phase Unwrapping (SNAPHU) (Chen and Zebker, 2000). Unwrapping errors are manually corrected, and the unwrapped phases are then converted to deformation in the radar's line-of-sight (LOS) direction.

Then InSAR derived surface deformations are used to constrain the fault geometry and static slip distribution. Here we assume that the pre- and post-seismic deformation can be ignored, as the earthquake source is deep and there is no foreshock and very few aftershocks (Ye et al., 2020). Quadtree down sampling method is applied to reduce the number of measurement points to ~500 for each image (J´onsson *et al.*, 2002). The earthquake is firstly modelled as a rectangle plane with nine parameters describing fault size, orientation, location and the uniform slip vector. The static Green's functions for a homogeneous elastic half-space are applied and the Poisson ratio is set to be 0.25 (Okada, 1985). To identify the ruptured fault plane, we set up the initial fault geometry with both east- and west-dipping directions based on the nodal planes from GCMT. We use the Geodetic Bayesian Inversion Software (GBIS) to search for the optimal source parameters of uniform slip model through the Bayesian approach (Bagnardi and Hooper, 2018). Then, based on the inverted optimal fault parameters with uniform slip, distributed slip inversions are performed using the

steepest decent method (SDM) with a least-square optimization (Wang *et al.*, 2011). Considering the depth of the 2019 Peru earthquake, a 1D layer velocity model extracted from Crust1.0 (Laske et al., 2013) is applied to calculate the Green's function for distributed slip model inversion. We extend the fault plane to 340 km-by-150 km for the east-dipping fault and 340 km-by-220 km for the west-dipping fault, and divide the planes into 10 km-by-10 km sub-faults.

2.2.2 Results

The derived InSAR images are coherent, despite the dense cover of the Amazon rainforest, with four coseismic interferograms in three tracks (descending tracks DT171, DT69 and ascending track AT120) showing clear fringes, probably thanks to the short revisit period (Figure 1b shows the region around the epicentre, Figure S2 shows all interferograms). Two interferograms in descending track DT69 are produced in this study including the 6-day interferogram (2019/05/23-2019/05/29) that covers only small portion of the coseismic deformation field but with shorter spanning time, i.e. higher coherence, and the 12-day interferogram (2019/05/23-2019/06/04) that covers larger area but with longer spanning time, i.e. lower coherence (Figure S2). These InSAR interferograms reveal an elliptical deforming pattern elongated in N-S direction (Figure 1b), with clear fringes spreading at least 450 km. Due to the large focal depth (122 km) and a normal faulting mechanism of the earthquake, the deformation pattern is relatively smooth, with a maximum displacement of ~19 centimetres, moving away from the satellite along the radar's line-of-sight direction.

The uniform slip inversion results on both fault planes are shown in Figure S3-4 as marginal posterior probability distributions, where the strikes/dips/rakes and centroid depths are highly consistent with the long period GCMT and W-phase solutions. For distributed slip inversions (Figure S5), the root-mean-square (RMS) misfits are 1.287 cm and 1.365 cm for the east- and west-dipping fault planes, respectively, which are somewhat comparable considering the possible errors caused by atmospheric delays and other error sources. Therefore, we cannot with certainty determine the ruptured fault plane from geodetic inversion alone. Comparable misfits are also obtained from teleseismic-only finite fault inversions for the two nodal fault planes in previous study (e.g., Liu and Yao, 2020). However, the ruptured fault plane can be discriminated by joint analysis of the epicentre (uncertainty of ~10 km), geodetic slip models and BP results. In the geodetic slip models, the slip distribution on the west-dipping fault plane shows two separate asperities located to the north and south of the hypocentre, respectively, indicating a bi-lateral rupture (Figure S5b and d). In contrast, slip on the east-dipping fault plane is mostly distributed to the north of the epicentre (Figure S5a and c), suggesting a unilateral northward rupture, highly consistent with the BP result (Figure 2). We therefore conclude that the 2019 M_w8.0 Peru earthquake ruptured unilaterally toward north on the east-dipping fault plane.

2.3 Joint finite fault model inversion

2.3.1 Data and method

Before joint inversion of geodetic and seismic data for the FFM of the earthquake, we refine the hypocentre depth of the mainshock using a reference event method. We carefully pick the first P-wave arrivals on 50 teleseismic ($30^\circ \sim 90^\circ$) stations that have good azimuthal coverage to the earthquake and relocate the hypocentre relative to the nearby 2011 M_w7.0 event (depth = 148 km, 7.641°S, 74.525°W, NEIC) through a grid search method.

Using the refined hypocentre, we derive FFM with the method developed by (Ji et al., 2002), which allows the joint inversion of seismic waveforms and static deformation data (e.g. InSAR). Since teleseismic and static data provide complementary constraints on the kinematic rupture process, joint inversion can greatly suppress trade-off among model parameters (e.g. Wei et al., 2011). We download teleseismic waveform data from IRIS (http://www.iris.edu) recorded by the Global Seismological Network (GSN), which was designed to study global seismology therefore has the most uniform spatial coverage that provides best teleseismic (30° - 90°) dataset for FFM inversion. We selected 36 P-waves and 18 SH-waves based on the data quality and azimuthal coverage. Instrument responses are removed from the raw waveform data and converted to displacement after a low-pass filtering with corner frequency of 1.0 Hz. Although 1Hz seems quite high frequency for deterministic inversion, the waveforms are dominated by relatively low frequency energy. We use the same down-sampled InSAR datasets as used in the previous static inversions. In the inversion, we solve for quadratic ramps in the InSAR data to correct for orbital errors.

To parameterize the finite fault model, we divide the rectangle fault plane into smaller sub-faults and solve for the slip amplitude and direction, risetime and rupture velocity on each sub-fault. For each parameter, we specify the bounds and a discretization interval. The bounds and increments of ?? are selected based on trial-and-error. We define the misfit function as:

$$E_{wf} + W_I \times E_I + W_S \times S + W_M \times M \quad (1)$$

where E_{wf} is the waveform misfit. E_I is the geodetic misfit, S is a normalized, second derivative of slip between adjacent patches (smoothing), M is a normalized seismic moment, and W_I, W_S and W_M are the relative weighting for the geodic misfit, smoothing, and seismic moment, respectively. In the joint inversion, the relative weighting is realized by normalizing the misfit of each dataset by the misfit derived by inverting the individual dataset. Here we test different values of W_I, and we found that by setting the weight for the geodetic misfits twice larger than the waveform misfits did not significantly degrade the fits to the teleseismic or geodetic data between the individual and joint inversions given the normalizations schemes. The static green's functions at free surface are calculated by using the same 1D velocity model from Crust1.0 (Laske *et al.*, 2013). We use a simulated annealing algorithm (Ji et al., 2002) to find the best

fitting model parameters for the joint inversions for coseismic slip. This nonlinear, iterative inversion algorithm is designed to avoid local minima by searching broadly through parameter space in initial steps, and then in later iterations to focus on regions that well fit the data.

Here we set the sub-fault size as 8 km × 6 km, constrain the rake angles to be between -110° to -70°, and allow rupture velocity to vary between 3.5 - 2.7 km/s, assume the risetime to be an arc of the cosine function and to vary between 1.0 and 19.5 s with 1.5 s steps. The slip amplitude can change from 0 to 6 m. Note that the selection of rupture speed range is guided by the BP results, this is critical for resolving the risetime of the rupture, as it reduces the trade-offs between rupture speed and risetime.

2.3.2 Results

The depth of the calibration event is well resolved by moment-tensor inversion using teleseismic waveform data, as depth phases are fitted decently (Figure S6a-e). Since a simple source-time-function can fit the waveform of the calibration event very well, we consider the source process of the event is relatively simple and compact, and therefore its hypocentre depth and centroid depth are nearly the same. We then refine the hypocentre of the Mw8.0 mainshock by minimizing the L2-norm error between the handpick travel-time residual of the event pair and the theoretical predictions. The grid search yields the best depth at 122 km (Figure S6f), which is coinciding with the NEIC report.

Based on the ruptured fault plane determined from geodetic inversion and the BP result, we adopt the strike (353°) and dip (57°) from the GCMT solution for the finite fault inversion. With the hypocentre depth refined by the calibration event at 122 km, we further refine the horizontal location of the hypocentre. We move the epicentre around the NEIC report (5.813°S, 75.2775°W) at the grid spacing of 0.1°, which is the approximate uncertainty of the NEIC location, and conduct joint inversion at each grid point to find the best location that minimizes misfits. We find that the epicentre at 5.913°S, 75.3775°W fits the data best (Figure S7), and we therefore use it for the following finite fault inversions. Thanks to the InSAR data, the absolute location of the epicentre is robust (e.g., uncertainty < 10 km). The accurate hypocentre and epicentre are essential to verify the two slab interface models: Slab1.0 (Hayes *et al.*, 2012) and Slab2 (Hayes *et al.*, 2018). As shown in Figure 1c and d, Slab1.0 model places the east-dipping fault plane within the subducted Nazca plate, while the fault plane is located in the mantle wedge in the Slab2 model. Therefore, we consider Slab1.0 as a better model for the Peru region, and use it to interpret and discuss our results.

With the refined epicentre we derived our preferred rupture model of the earthquake. The depth profile of the rupture model is presented in Figure 3b-d, along with the corresponding moment-rate functions (Figure 3a, grey zones). The waveform and InSAR data fits can be found in Figure S8 and Figure S9. Excellent fits between the data and synthetics indicate the robustness of the inversion.

To further verify the resolution of the inversion, we conduct checkerboard tests for the inversion setups. We generate synthetic data for checkerboard-like slip models and invert these synthetic data with the same inversion parameters as we apply to the real data (Figure S10). The results indicate that the model has good and relatively uniform resolution to the rupture area of the earthquake. We note that the spatial resolution is slightly worse in the middle of the model than the edges, which is related to the extreme checkerboard like input slip model, as the middle of the model has stronger contrast with the nearby slip patches compared with the edges of the model. The rise time recovery is presented in Figure S10d, which shows reasonable agreement with the input model (about ± 2s variation around the input value). In general, rise time is more difficult to be resolved in checkerboard test, as it is a quite extreme case, where zero slip patch is located next to the largest slip patches. To show the resolution to the rise time in a more realistic scenario, we conduct another resolution test (Figure S11), in which we use four major slip patches, which better mimic the slip distribution of the real earthquake (Figure 2), to generate the synthetic data. It shows that we can well resolve the rise time of each slip patch (Figure S11). We notice that the last slip patch has slightly worse resolution than the earlier asperities, which is caused by the interferences from the earlier rupture to the later rupture.

We also conduct another checkerboard test to show the contribution of InSAR data in the inversion (Figure S12). The main difference between the joint inversion and teleseismic only inversion is the slip amplitude of the asperities and the sharpness of asperity boundary. The improvement from the InSAR data is not as dramatic as that for the shallow earthquakes, but this is not unexpected, as the InSAR data resolution reduce as the depth of earthquake increases. The west dipping fault plane can be ruled out easily, as teleseismic waveform fits are much worse than the east dipping fault (Figure S13).

The preferred joint inversion model on the east dipping fault plane shows a clear northward rupture directivity (Figure 2 and Figure 3), with an average rupture speed of ~3.0 km/s, as constrained by the value from BP. The rupture model displays multiple asperities along strike, spatially highly consistent with the H1-H4 clusters from the BP result. We name these asperities as S1-S4, with the numbers indicating both the propagation from south to north and their rupture in time (Figure 3). S1 corresponds to the rupture near the hypocentre in the first 14 s, and has a M_w of 7.40. S2 is located at about 60 km north of S1, and has a M_w of 7.35, with its rupture starting at ~20 s after the origin time. The largest asperity S3 (M_w7.70) follows S2 closely in both space and time, corresponding to the peak slip (4 m) in the model. The last asperity, S4, (M_w7.45) follows S3 immediately, and extends the rupture further north, terminating at the latitude of ~4.3° S, and corresponding to the rupture from 45 to 60 s. The finite fault model defines a total rupture length of 200 km and a duration of ~60 s (Figure 2). Note that the same velocity model is used in hypocentre refinement, centroid depth inversion of the reference event and FFM inversion, therefore the relative location between the hypocentre and the asperities are robust.

Interestingly, there is almost no slip between S1 and S2, indicating that the rupture almost completely stopped between these two asperities. This can be verified by a careful inspection on the azimuthal profile of the displacement record section for this quiet zone (Figure 4a). Assuming a depth of 122 km, the depth phases of S1 would have arrived later than 30 s after the rupture started, therefore the first 20 s of the waveform records are dominated by direct down-going P waves. For stations that sampled the strongest negative P-wave radiation pattern (e.g., North American stations), the P-wave displacement should be either negative (corresponding to rupture) or zero (corresponding to no or very little rupture). Accordingly, the displacements of the North American array stations almost fall back to zero between S1 and S2 (indicated by the dashed line in Figure 4a), which further supports a very limited rupture or even no slip between S1 and S2.

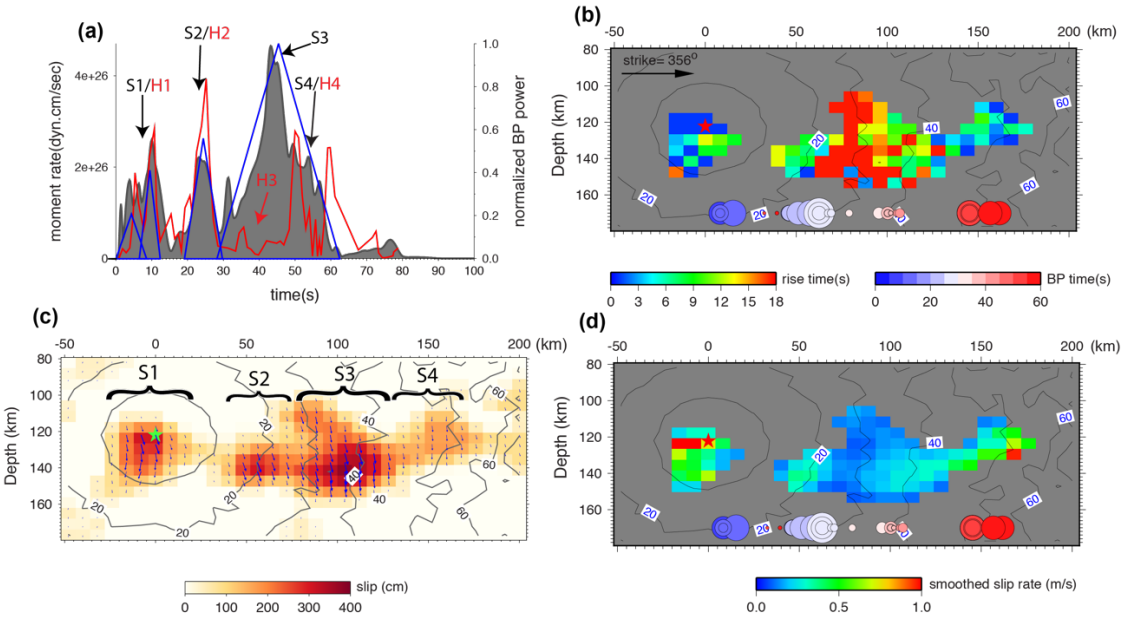

Figure 3. Rupture process derived from joint inversion using geodetic InSAR and teleseismic waveform data. (a) The moment-rate function of the preferred FFM (black) overlaps with the normalized BP power (red) from the North American array at 0.2-1.0 Hz and moment rate from the MPS result (blue). (b) The risetime distribution of the model in depth profile and the BP result are presented at the bottom as a function of time and distance away from the epicentre. Note that as BP does not have depth resolution, the BP result does not correspond to any depth. The contours indicate the rupture time of the model. (c) Depth profile of the slip distribution. The arrows indicate the rake angles. (d) Smoothed slip-rate, defined as slip over risetime, distributed on the depth profile.

2.4 Multiple point source inversion

2.4.1 Data and method

To investigate the variability of fault geometry during the rupture for the 2019 Peru earthquake, we also perform a multiple point source (MPS) inversion which allows the variability of fault geometry of subevents and focuses more on the first-order complexity of the rupture process. The MPS inversion method (Shi *et al.*, 2018) we use here takes advantages of the Cut-and-Paste (CAP) waveform modelling scheme (Zhao and Helmberger, 1994; Zhu and Helmberger, 1996) and the Markov-Chain-Monte-Carlo sampling algorithm. By cutting the teleseismic waveforms into P- and S-wave time window and allowing different time shifts to align them with synthetics, the inversion relies less on the accuracy of the velocity model and hence can be performed in relatively higher frequency range. Due to much fewer parameters than those in a finite fault model, the MPS method can avoid overfitting the data.

We run the MPS inversion iteratively to gradually increase the number of subevents, therefore the optimal MPS model should have appropriate number of parameters that adequately model the waveform. Here we use the 1D IASP91 velocity model to compute the Green's functions by the FK method (Zhu and Rivera, 2002). The reliability of the Green's functions is validated with a path calibration technique that has been demonstrated to be very useful in previous studies (Wei *et al.*, 2015; Wei *et al.*, 2018; Wei *et al.*, 2013). A good calibration event is selected in the source region, of which the rupture process should be as simple as a point source within the frequency range that is meaningful for resolving the detailed rupture process of the target event (i.e., the 2019 M_w8 Peru earthquake). Once the calibration event is selected, the calibration is done by conducting point-source moment tensor inversion using the CAP method (Zhao and Helmberger, 1994; Zhu and Helmberger, 1996). Because the site conditions and ray paths to the stations are different, we apply different filtering frequency ranges for P and S waves on different stations. In general, the frequency range is 0.01-0.2 Hz for P-waves and 0.01 – 0.15 Hz for S-waves. We then use the waveform cross-correlation and misfit between data and synthetics to select the components that can be well modelled. We discard the stations that are close to other stations to avoid the station coverage being dominated in a certain azimuthal range. In this study, we conduct path calibration with nearby 2011 M_w7.0 event (7.641°S, 74.525°W, NEIC). We select P and S waves from 47 IRIS (http://www.iris.edu) stations that are relatively evenly distributed in azimuth, for which the Green's functions are reliable at the calibrated frequency ranges. In the MPS inversion for the target earthquake, we apply the P and S time shifts for aligning the data with synthetics of the calibration event to the time correction of the MPS synthetics, which greatly reduce the uncertainty of the inversion results.

2.4.2 Results

Through multiple inversions, we find that four sources are required to adequately model the teleseismic waveforms (Figure 2, red beach balls numbered 1-4 and Figure S14). Their moment magnitudes are Mw7.01, Mw7.10, Mw7.36, and

Mw7.87, and their centroid depths are 133 km, 135 km, 140 km, and 139 km, respectively (see Figure S15 for the uncertainties of the source parameters). Note that these depths are ~15 km deeper than the refined hypocentre (122 km), indicating the earthquake likely started within the oceanic crust and rupture propagated to the upper mantle of the subducted slab. The moment-rate function from MPS is highly consistent with that from FFM (Figure 3a, triangles). The first and second subevents together match S1 in FFM, as shown in both the map view and moment-rate functions (Figure 2 and Figure 3a). The third subevent matches S2 in FFM and the largest, fourth, subevent corresponds to S3 in FFM. MPS cannot resolve S4 as well as FFM can, partly because the MPS inversion is dominated by longer period waveforms than FFM while S4 is characterized by higher-frequency rupture following the largest low-frequency asperity S3, therefore the coda wave of S3 could have contaminated the direct waves of S4.

Although the MPS solution resolves the first order rupture directivity well, the horizontal locations of the third and fourth subevents are ~20 km further to the north of the corresponding asperities in FFM (Figure 2). This is likely caused by the uniform source time function applied to all the stations in the MPS inversion, which is insufficient to approximate the rupture directivity of each subevent, and hence the inversion is compensated by location shifts in the rupture direction. We do not see dramatic fault geometry variation but find that the strike of the first subevent is 20°, and gradually rotates counter clockwise to 353° for the northernmost subevent. All subevents have pure normal-faulting focal mechanisms except for the first subevent, which has some left-lateral strike-slip component. The geometry difference between the first and the following subevents indicates a relatively heterogenous stress status or fault structure near the hypocentre compared with the subsequent rupturing areas. Considering the fault geometries of the later ruptures are relatively uniform, such an intermediate-depth earthquake may involve a relatively complex nucleation process, after which the rupture is dominated by a pure normal-faulting mechanism, facilitated by a dynamic weakening mechanism as discussed later.

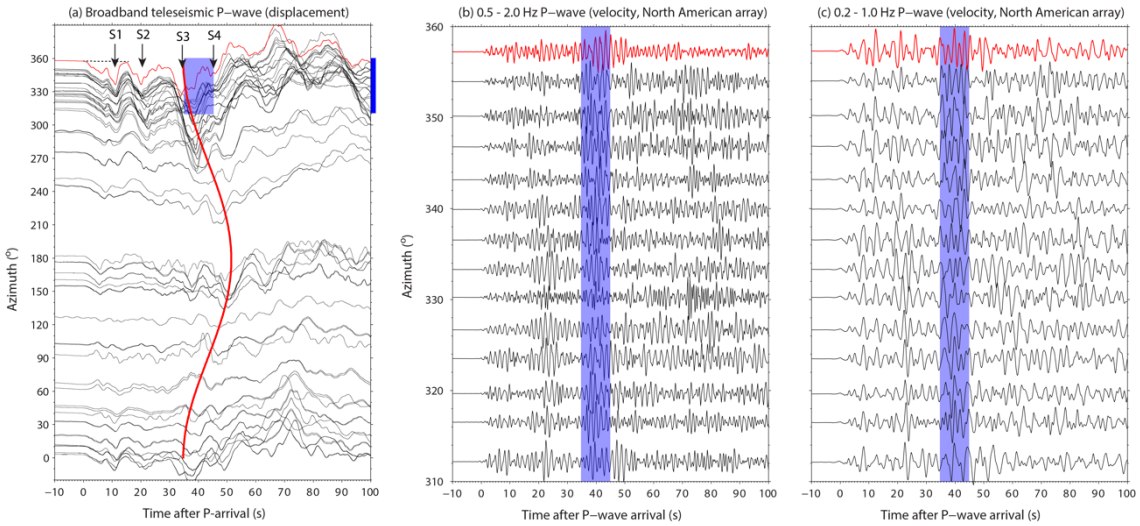

Figure 4. Comparison between broadband and high-frequency waveforms. (a) Displacement waveforms of teleseismic P-waves recorded by GSN stations, which is dominated by low-frequency energy. (b) 0.5—2.0 Hz and (c) 0.2—1.0 Hz velocity waveforms of down-sampled North American array stations. The thick red line in (a) indicates the arrival of energy from the largest coseismic asperity (S3 in Figure 3) in different azimuths. The blue shadows in (b) and (c) mark the identified high frequency energy following the largest low-frequency energy and bursting around 40 s after the P-wave arrival. The red waveforms are recordings from the SSPA station (location is shown in Figure 1 inset and Figure S1a), which will be further analysed in Figure 5.

3. Frequency dependent rupture

The agreement in timing and location (horizontal) between HF-clusters (H1-H4) derived from BP and asperities (S1-S4) inferred from FFM (Figure 2 and Figure 3) confirms that our results are robust. Intriguingly, BP and FFM results show striking contrasts between H3 and S3, where the BP result indicates a very weak HF-energy (H3) radiated from the largest asperity (S3) in the FFM (Figure 3a). This contrast thus clearly indicates a frequency-dependent rupture and can be explained by another contrast: the risetime contrast between S3 and the other asperities (S1, S2 and S4) (Figure 3b). The FFM risetime for S3 is 4-8 times longer than that for the other asperities, while the peak slip ratio of S3 and each remaining asperity is less than 2. The ultra-long risetime of S3 (~15 s) could be interpreted as a smooth and low slip-rate rupture process which therefore radiated much weaker HF-seismic waves (Figure 3d). We conducted another FFM inversion in which the maximum rise time allowed is 9 s (Figure S16). We notice that the waveform and InSAR data fitting is only slightly worse than the preferred model, but the rise time for S1 and S2 are still much shorter than S3. Therefore, we consider the rise time contrast between S3 and other asperity is a robust feature, but the absolute rise time value of S3 is less well constrained.

Both rupture models could be found in the supplementary materials.

To further verify the frequency-dependent strength contrast between S3 and the other asperities, we inspect the spectrum of teleseismic P-waves recorded by the North American stations. We select a representative station, SSPA (azimuth = 357°, distance = 46.32°, Figure 1 inset and Figure S1a), for the spectrogram analysis. In Figure 5, the arrival times of low-frequency energy from S1-S4 can be clearly identified from the displacement waveform and the corresponding spectrum. The peak displacement, generated by S3, arrived ~32 s after the P-wave onset. Note that the unilateral northward rupture propagating at 3.0 km/s caused the peak displacement to arrive at the SSPA station ~10 s earlier than the peak in the moment-rate function (describing the energy release on the fault), as S3 is ~100 km closer to SSPA compared with S1. The HF-spectrum (0.5-2.0 Hz and 0.2-1.0 Hz), on the other hand, clearly shows that the largest amplitude arrived around 42 s after the P-wave onset, ~10 s later than the arrival of the low-frequency energy of S3 (Figure 5). Based on the timing and rupture directivity, this largest high-frequency energy corresponds to S4, rather than S3, as it arrived much later. As shown in Figure 4, the SSPA waveform is similar to waveforms recorded by other North American array stations, therefore represents a robust feature of the data. This spectrum analysis confirms the relatively weak HF-strength of S3, as shown in both the beamforming of BP and moment rate function of FFM (Figure 3a).

In addition to this single station detailed waveform analysis, the stacked waveforms of the North America array in azimuthal profiles also shows clear contrast of high frequency radiation between S3 and other asperities (Figure 6). The timing and amplitude of low frequency (< 0.2 Hz) envelopes of the stacked high-frequency waveform agree very well with the displacement waveform in the first 30s (peak-to-peak, trough-to-trough), indicating similar timing and location of high and low frequency seismic sources. But dramatic difference is shown for S3, where the envelope amplitude is much weaker than the displacement. The peak amplitude of the envelope appears at the timing of S4, 4 – 5s later than the arrival time of peak displacement waveform (S3). The stacked envelopes of the high frequency waveforms show different amplitude ratio between the beginning part of the rupture and the later larger asperities, which is well consistent with the shorter rise time (or larger slip-rate) for the beginning part of the rupture. In contrast with the displacement waveform, the depth phase is almost invisible in the envelopes, likely caused by stronger attenuation for high frequency pP and sP phases. This also support that our BP result is less affected by the depth phases.

The power derived from our BP result is at odds with the power derived in a previous study (Liu and Yao, 2020), in which the Alaska array data were used. Their results show that the peak of the HF-energy arrival time is 42 s, 10 s earlier than the timing of H4, which clearly does not agree with the power spectrum analysis for SSPA as well as array stacked waveform analysis, possibly because they didn't consider the rupture directivity of the earthquake

and thus mis-located the timing of the maximum BP power and the moment-rate function. Ye *et al.* (2020) has similar BP result with Liu and Yao (2020) and the BP signals after 50 s are ignored. Noted that in these published BP analysis, no path calibration was conducted. The slip distribution of our result and the published FFMs are quite similar, but our rise time resolution is better as geodetic data and rupture speed constraints from BP allow us to better resolve rise time variation of the earthquake.

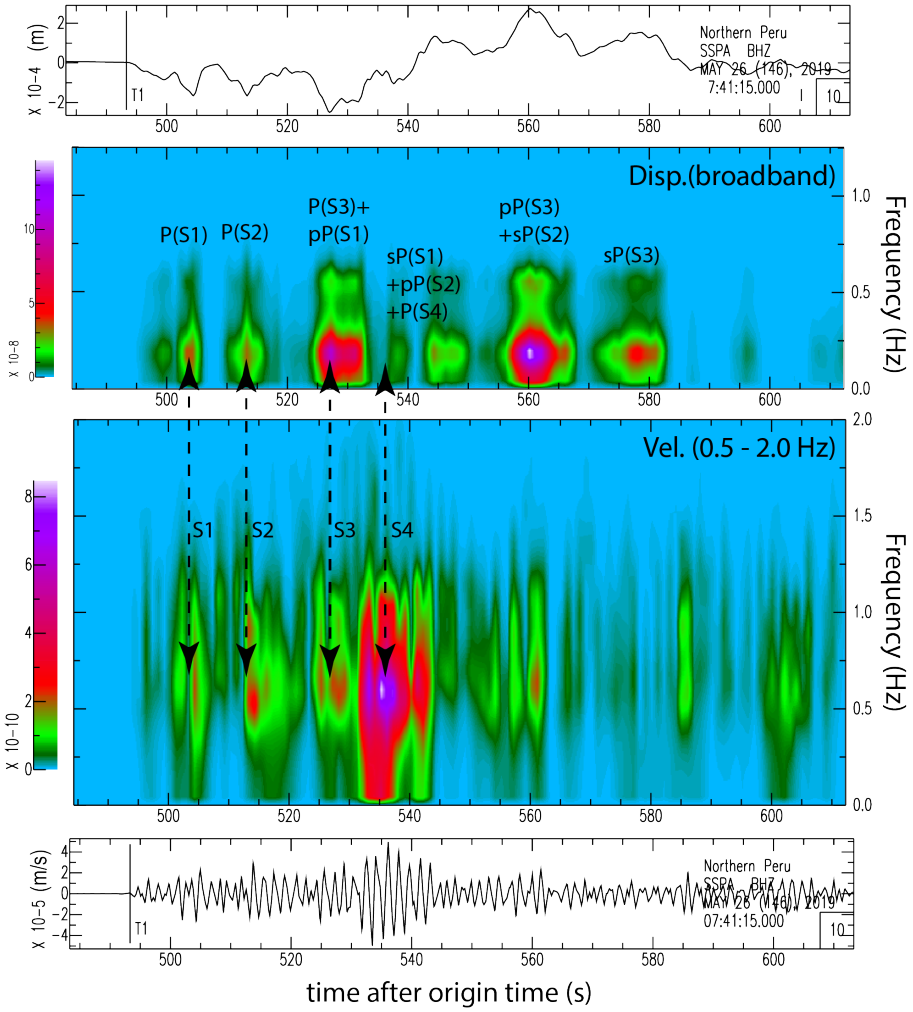

Figure 5. Spectrogram at the SSPA station (the red waveform trace in Figure 4a). The broadband displacement waveform is shown at the top, followed by the spectrogram of displacement and velocity (0.5-2.0 Hz). The velocity waveform filtered to 0.5 - 2.0 Hz is presented at the bottom. The arrows indicate the arrivals of key asperities. P-wave (P) and the depth (sP and pP) phases of these asperities are indicated in the displacement spectrogram as well. Note the

different arrival times of S4 at low and high frequencies.

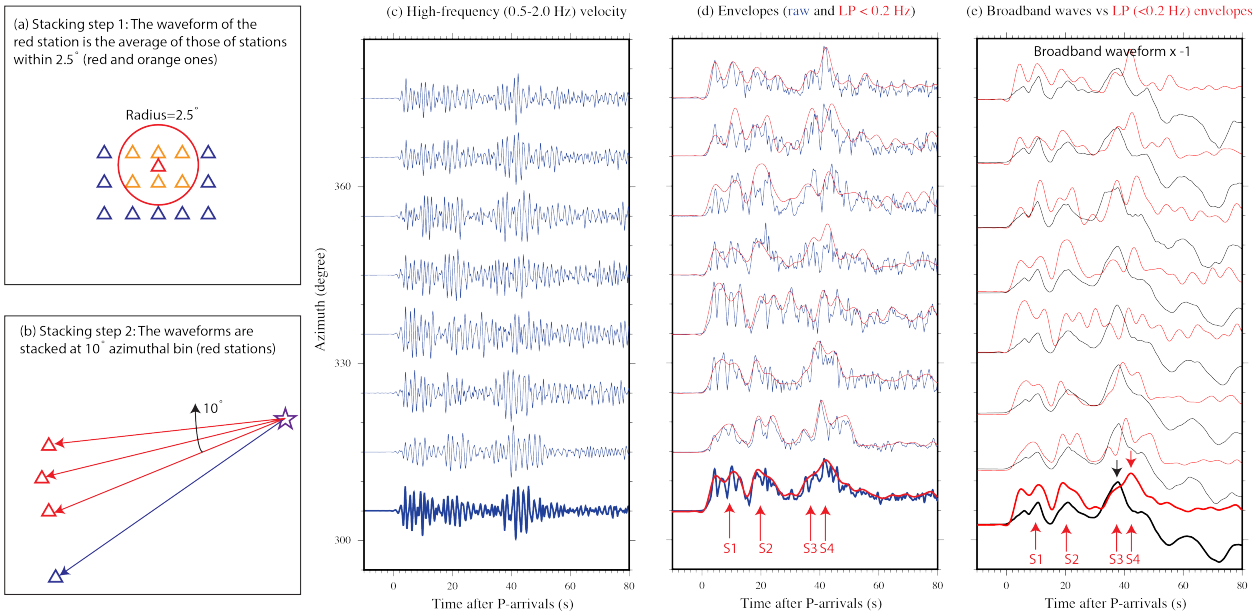

Figure 6. Stacked North America array waveforms. (a-b) Illustration of the two steps stacking strategy, with the first step in a 2.5° circle (a) and then in an azimuthal bin of 10° (b). (c) Azimuthal profile of stacked high frequency (0.5 – 2.0 Hz) velocity waveform for the North America array. The bottom heavier traces are the stacked of all the waveforms in the profile (same for (d) and (e)). (d) Raw envelope (blue) and low pass filtered (< 0.2 Hz) envelope (red) of high frequency waveforms in (c). The arrows indicate the subevents (S1 - S4) identified in Figure 4 and 5, note that the largest amplitude is produced by S4. (e) Comparison between the stacked displacement waveforms (black) and the low pass filtered (< 0.2 Hz) envelopes (red). The smaller arrows indicate the largest amplitudes in displacement waveform (S3, black arrow) and high frequency envelope (S4, red arrow).

4. Discussion and Conclusions

The strike (356 º) of the 2019 M_w8.0 northern Peru earthquake is consistent with the orientation of the linear bathymetric features near the trench, and is also similar to the strike (near N-S direction) of outer-rise normal faulting focal mechanisms. The ruptured fault plane determined in this study dips to the east, as do the majority of outer-rise faults in a region that is ~1500 km further to the north (Ranero *et al.*, 2003). The moment tensors of earthquakes near the 2019 M_w8.0 event (Figure 1a and inset of Figure 7) have very similar normal faulting focal mechanisms, which is in contrast to other intermediate-depth intraslab earthquakes in south America where more diverse focal mechanisms are found (Warren, 2014). These observations point to a reactivation of an outer-rise

normal fault (Jiao et al., 2000) during the 2019 Peru event.

This reactivated fault ruptured both the shallow and deeper seismicity zones, which separated by ~16 km as revealed in (Brudzinski *et al.*, 2007), and the area between them, based on the vertical extent of the rupture (up to 25 km) in our preferred model, suggesting a dynamic weakening mechanism during the earthquake. Here, we argue that such a dynamic weakening mechanism is most likely thermal pressurization (TP) of pore fluid for the following reasons. First, observations for the largest asperities in several well-resolved shallow earthquakes that show longer risetime, smoother ruptures and lack of high-frequency radiation, such as Ma *et al.* (2003) for Chi-Chi earthquake and Wei *et al.* (2012) for Tohoku-Oki earthquake, similar to S3 in our model. These observations have been interpreted as an effect of TH (e.g., Wei *et al.*, 2012; Tanikawa and Shimamoto, 2009; Noda and Lapusta, 2013). Second, these features have been reproduced by earthquake dynamic simulations considering TP of pore fluid (Noda and Lapusta, 2010). Third, laboratory experiments on rock samples from fault zones also confirm that slip weakening can be produced by TP (Wibberley and Shimamoto, 2005; Tanikawa and Shimamoto, 2009), although such experiments have not yet been conducted on serpentinite. Fourth, given the temperature and pressure at the depth of the 2019 Peru earthquake, dehydration of the oceanic crust and the upper portion of the mantle lithosphere supplies free water to the porous rock (Ranero *et al.*, 2003) as a pre-condition for TP, meaning that the rupture mechanism of the 2019 earthquake can be explained by the dehydration embrittlement hypothesis (e.g. Green and Houston, 1995). Although existence of free water at such depths is sometimes disputed (e.g. Kohlstedt *et al.*, 1996), it is generally agreed on (e.g. Green and Houston, 1995; Hacker *et al.*, 2003). Fifth, permeability of the hydrous serpentinite at the depth of the earthquake is sufficiently low in the lithosphere mantle (Hatakeyama *et al.*, 2017) to allow TP of pore fluid to take place.

With the above-mentioned arguments in favour of TP as the dynamic weakening mechanism of the 2019 M_w8.0 northern Peru earthquake, we also highlight that our study expands the TP mechanism to intra-slab earthquakes at intermediate depths, that is, to earthquakes not included in the extensive dataset compiled based on fracture energy by (Viesca and Garagash, 2015).

It is unlikely that the ductile shear instability mechanism played a role during the 2019 Peru earthquake. The hypocentre of the earthquake (122 km as in Figure S6), which was ~15 km shallower than the centroid of sub-events in the MPS solution and asperities in FFM (Figure 3), was likely located within the oceanic crust or the uppermost lithosphere mantle in the upper seismicity zone. This portion of the slab has a temperature of less than 400 °C (Figure 7) (Hu and Liu, 2016; Stadler et al., 2010), much lower than the temperature needed for ductile shear instabilities caused by heating (600 - 800 °C) (Kelemen and Hirth, 2007). Actually, most of the slip of the Peru earthquake took place in the fault area whose temperature is lower than 600-700 °C (Figure 7), and slip was confined within a vertical rupture width of ~25 km (Figure 3), less than half

of that revealed for the 2013 Khash, Pakistan, intra-slab earthquake (Barnhart *et al.*, 2014). Such a narrow rupture width is expected, given that the Nazca plate (~30 Ma old) is much younger than the Makran slab (~80Ma old) that hosted the Khash earthquake. Therefore, the ~650 °C isothermal depth relative to the subducted oceanic floor in the Nazca plate is much shallower than that of the Makran slab (Figure 7). This suggests that the thermal structure of 650 °C controlled the depth range of the rupture, consistent to the extensive dataset compiled for shallower intraplate earthquakes (McKenzie *et al.*, 2005).

The 2019 M_w8.0 event was located further east of all other nearby intra-slab normal faulting earthquakes (Figure 7 inset), where the slab begins to bend and dip into deeper mantel. The T-axis components of all these intra-slab events are mainly along the downdip direction of slab, showing tensional stress in this part of the slab (Figure 7 inset). The slip of the 2019 Peru event rupture was located mostly above the mid-plane (derived from a geodynamic modelling result of Sandiford *et al.*, 2019), defined as the boundary between extensional stress above and compressional stress below it. Based on the geodynamic modelling, intra-slab normal faulting earthquakes could be largely explained by the downdip curvature gradient of the slab, yet, the 2019 Peru event is an outlier (Figure 8 in Sandiford *et al.*, 2019). In fact, the moment of the 2019 event was larger than the sum of the moments of all previous nearby earthquakes in the NEIC catalog. We therefore argue that the stress status within the seismogenic portion of the slab is better represented by the largest earthquakes, and we suggest that the slab-pull force was the driving factor that produced the 2019 event. The slab-pull interpretation is also adopted by Liu and Yao (2020) in their study of the 2019 event.

We calculate the static stress drop distribution from our preferred model for the 2019 Peru event (Figure S18), by implementing the method proposed by Ripperger and Mai (2004). The slip-weighted average stress drop derived in this way is ~6 MPa, which is only a third of that derived for the 2005 Mw7.8 intra-slab Tarapaca earthquake (Delouis and Legrand, 2007). Similarly, the 2019 Mw7.5 intra-slab event, which occurred several hundred kilometers to the north, also shows more compact slip distribution compared with the Mw8.0 event (https://earthquake.usgs.gov/earthquakes/eventpage/us2000jlfv/finite-fault). Such diversity in stress drop calls for further studies along with the frequency dependent feature of the rupture, as the spectrum of earthquake energy radiation is closely related to its stress drops. The seismological approach adopted in this study can be applied to other large intermediate-depth and deep-depth earthquakes to further investigate their frequency dependent ruptures, as well as to verify the universality of the TP mechanism.

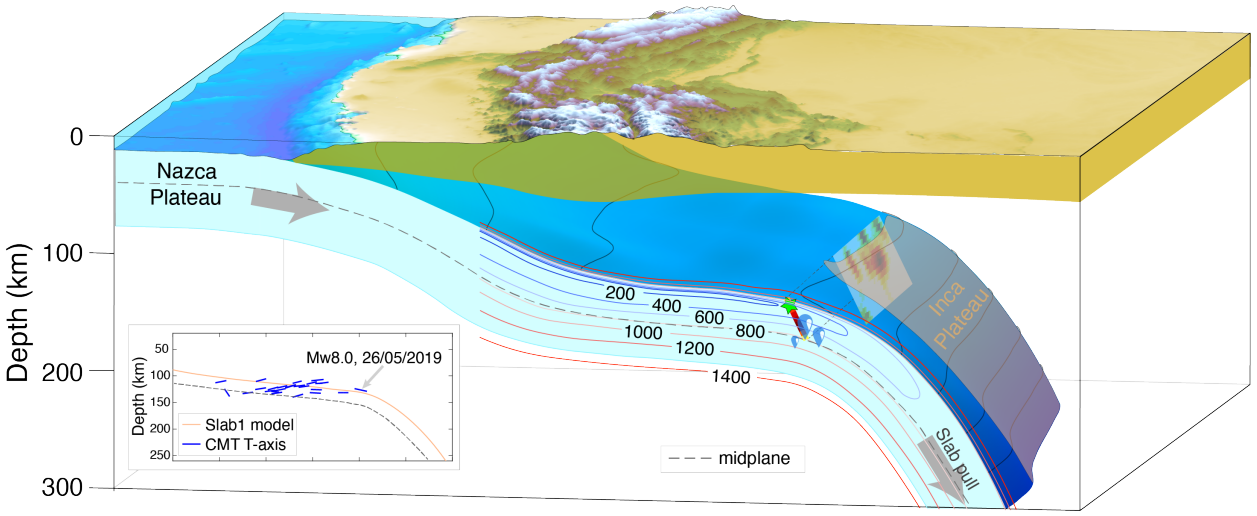

Figure 7. Schematic map of the 26 May 2019 Peru earthquake and subducted Nazca slab in Peru. Thermal structure is represented by coloured lines (details of thermal structure model (Stadler et al., 2010) are shown in Figure S17). The inset shows the projection of CMT events in this region on a vertical cross-section in the schematic map. Dashed line shows the midplane. Green star in slip projection on the profile represents the hypocentre of the earthquake.

Acknowledgments

We thank Dr. Ting Yang for helpful discussion and Pavel Adamek for help in polishing the writing. We thank the editor, associate editor and anonymous reviewers for their constructive comments that improve the paper. All seismic data were downloaded through the IRIS Wilber 3 system (https://ds.iris.edu/wilber3/), including the following seismic networks: (1) the IU (GSN; Albuquerque, 1988), (2) II (Scripps Institution of Oceanography, 1986), (3) G (doi:10.18715/GEOSCOPE.G). The figures are plotted using the Generic Mapping Tools (GMT), Matlab and the Seismic Analysis Code (SAC). Part of the seismic data are processed using the SAC and the Python package, AIMBAT. Copernicus Sentinel data 2019. Retrieved from ASF DAAC 10th July, 2019, processed by European Space Agency. The down sampled InSAR data could be found in the supplementary materials. This study was supported by NSFC 41974017, and EOS internal research grant 04MNS001909A620 and Singapore MOE tier-2 grant MOE2019-T2-1-182.

References

Albuquerque Seismological Laboratory (ASL)/USGS. (1988). Global Seismograph Network (GSN - IRIS/USGS). International Federation of Digital Seismograph Networks. https://doi.org/10.7914/SN/IU

https://doi.org/10.1016/j.epsl.2016.06.019

https://doi.org/10.1016/j.epsl.2005.02.005

https://doi.org/10.1016/j.epsl.2020.116528

Avouac, J. P., L. Meng, S. Wei, T. Wang, and J. P. Ampuero (2015), Lower edge of locked Main Himalayan Thrust unzipped by the 2015 Gorkha earthquake, *Nature Geoscience*, *8*(9).Bagnardi, M., and A. Hooper (2018), Inversion of Surface Deformation Data for Rapid Estimates of Source Parameters and Uncertainties: A Bayesian Approach, *Geochemistry Geophysics Geosystems*, *19*(7), 2194-2211.Barnhart, W. D., G. P. Hayes, S. V. Samsonov, E. J. Fielding, and L. E. Seidman (2014), Breaking the oceanic lithosphere of a subducting slab: The 2013 Khash, Iran earthquake, *Geophys Res Lett*, *41*(1), 32-36, doi:10.1002/2013gl058096.Brudzinski, M. R., C. H. Thurber, B. R. Hacker, and E. R. Engdahl (2007), Global Prevalence of Double Benioff Zones, *Science*, *316*(5830), 1472, doi:10.1126/science.1139204.Chen, C. W., and H. A. Zebker (2000), Network approaches to two-dimensional phase unwrapping: intractability and two new algorithms, *Journal of the Optical Society of America A*, *17*(3), 401-414, doi:10.1364/JOSAA.17.000401.Chen, Y., L. Wen, and C. Ji (2014), A cascading failure during the 24 May 2013 great Okhotsk deep earthquake, *Journal of Geophysical Research: Solid Earth*, *119*(4), 3035-3049, doi:10.1002/2013jb010926.Delouis, B., and D. Legrand (2007), Mw 7.8 Tarapaca intermediate depth earthquake of 13 June 2005 (northern Chile): Fault plane identification and slip distribution by waveform inversion, *Geophys Res Lett*, *34*(1), doi:10.1029/2006gl028193.Ekstrom, G., M. Nettles, and A. M. Dziewonski (2012), The global CMT project 2004–2010: Centroid-moment tensors for 13,017 earthquakes, *Physics of the Earth and Planetary Interiors*, *200*, 1-9.Goldstein, R. M., and C. L. Werner (1998), Radar interferogram filtering for geophysical applications, *Geophys Res Lett*, *25*(21), 4035-4038.Green, H. W., and H. Houston (1995), The Mechanics of Deep Earthquakes, *Annual Review of Earth and Planetary Sciences*, *23*(1), 169-213.Hacker, B. R., S. M. Peacock, G. A. Abers, and S. D. Holloway (2003), Subduction factory 2. Are intermediate-depth earthquakes in subducting slabs linked to metamorphic dehydration reactions?, *Journal of Geophysical Research: Solid Earth*, *108*(B1).Hatakeyama, K., I. Katayama, K.-i. Hirauchi, and K. Michibayashi (2017), Mantle hydration along outer-rise faults inferred from serpentinite permeability, *Scientific Reports*, *7*(1), 13870, doi:10.1038/s41598-017-14309-9.Hayes, G. P., M. G. L., P. D. E., H. Mike, F. Hanna, F. Maria, and S. G. M. (2018), Slab2, a comprehensive subduction zone geometry model, *Science*, eaat4723-.Hayes, G. P., D. J. Wald, and R. L. Johnson (2012), Slab1.0: A three-dimensional model of global subduction zone geometries, *Journal of Geophysical Research*, *117*.Zeng, H.Y., S. J. Wei, and W. Wu (2019), Sources of uncertainties and artefacts in back-projection results, *Geophysical Journal International*(2), 2.Houston, H., H. M. Benz, and J. E. Vidale (1998), Time functions of deep earthquakes from broadband and short-period stacks, *Journal of Geophysical Research*, *103*, 29895-29913.Hu, J., and L. Liu (2016), Abnormal seismological and magmatic processes controlled by the tearing South American flat slabs, *Earth Planet Sc Lett*, *450*, 40-51,

doi:.Hu, Y., Yagi, Y., Okuwaki, R. and Shimizu, K., 2021. Back-propagating rupture evolution within a curved slab during the 2019 M w 8.0 Peru intraslab earthquake. Geophysical Journal International, 227(3), pp.1602-1611.Ishii, M., P. M. Shearer, H. Houston, and J. E. Vidale (2005), Extent, duration and speed of the 2004 Sumatra–Andaman earthquake imaged by the Hi-Net array, *Nature*, *435*(7044), 933-936, doi:10.1038/nature03675.J´onsson, S. o., H. Zebker, P. Segall, and A. Falk (2002), Fault slip distribution of the 1999 Mw7.1 Hector Mine, california, earthquake, estimated from satellite radar and GPS measurements, *Bulletin of the Seismological Society of America*, *92*(4), 1377-1389.Ji, C., Wald, D.J. and Helmberger, D.V., 2002. Source description of the 1999 Hector Mine, California, earthquake, part I: Wavelet domain inversion theory and resolution analysis. Bulletin of the Seismological Society of America, 92(4), pp.1192-1207.Jiang, H., G. Feng, T. Wang, and R. Bürgmann (2017), Toward full exploitation of coherent and incoherent information in Sentinel-1 TOPS data for retrieving surface displacement: Application to the 2016 Kumamoto (Japan) earthquake, *Geophys Res Lett*, doi:10.1002/2016gl072253.John, T., S. Medvedev, L. Rupke, T. B. Andersen, Y. Y. Podladchikov, and H. Austrheim (2009), Generation of intermediate-depth earthquakes by self-localizing thermal runaway, *Nature Geoscience*, *2*(2), 137-140.John, T., and V. Schenk (2006), Interrelations between intermediate-depth earthquakes and fluid flow within subducting oceanic plates: Constraints from eclogite facies pseudotachylytes, *Geology*, *34*(7), 557-560.Jung, H., H. W. Green Ii, and L. F. Dobrzhinetskaya (2004), Intermediate-depth earthquake faulting by dehydration embrittlement with negative volume change, *Nature*, *428*(6982), 545-549, doi:10.1038/nature02412.Kelemen, P. B., and G. Hirth (2007), A periodic shear-heating mechanism for intermediate-depth earthquakes in the mantle, *Nature*, *446*(7137), 787-790.Kirby, S. H., E. R. Engdahl, and R. Denlinger (1996), Intermediate-depth intraslab earthquakes and arc volcanism as physical expressions of crustal and uppermost mantle metamorphism in subducting slabs, *Geophysical monograph*, *96*, 195-214.Kohlstedt, D. L., H. Keppler, and D. C. Rubie (1996), Solubility of water in the , and phases of (Mg,Fe)2SiO4, *Contributions to Mineralogy and Petrology*, *123*(4), 345-357.Kreemer, C., G. Blewitt, and E. C. Klein (2014), A geodetic plate motion and Global Strain Rate Model, *Geochemistry, Geophysics, Geosystems*, *15*(10), 3849-3889, doi:10.1002/2014gc005407.Laske, G., G. Masters, Z. Ma, and M. Pasyanos (2013), Update on CRUST1. 0—A 1-degree global model of Earth's crust, paper presented at Geophys. Res. Abstr.Liu, W., and H. Yao (2020), Rupture Process of the 26 May 2019 Mw 8.0 Northern Peru Intermediate-Depth Earthquake and Insights Into Its Mechanism, *Geophys Res Lett*, *47*(4).Ma, K.F., Brodsky, E.E., Mori, J., Ji, C., Song, T.R.A. and Kanamori, H., (2003). Evidence for fault lubrication during the 1999 Chi-Chi, Taiwan, earthquake (Mw7. 6). *Geophysical Research Letters*, 30(5).McKenzie, D., J. Jackson, and K. Priestley (2005), Thermal structure of oceanic and continental lithosphere, *Earth Planet Sc Lett*, *233*(3), 337-349,doi:.Melgar, D., et al. (2018), Deep embrittlement and complete rupture of the lithosphere during the Mw 8.2 Tehuantepec earthquake, *Nature Geoscience*, *11*(12), 955-

960, doi:10.1038/s41561-018-0229-y.Meng, L., J. P. Ampuero, Y. Luo, W. Wu, and S. Ni (2012), Mitigating artifacts in back-projection source imaging with implications for frequency-dependent properties of the Tohoku-Oki earthquake, *Earth Planets & Space*, *64*(12), 1101-1109.Muller, R. D., M. Sdrolias, C. Gaina, and W. R. Roest (2008), Age, spreading rates, and spreading asymmetry of the world's ocean crust, *Geochemistry Geophysics Geosystems*, *9*(4).Noda, H., and N. Lapusta (2010), Three-dimensional earthquake sequence simulations with evolving temperature and pore pressure due to shear heating: Effect of heterogeneous hydraulic diffusivity, *Journal of Geophysical Research: Solid Earth*, *115*(B12),doi:10.1029/2010jb007780.Noda, H. and Lapusta, N., 2013. Stable creeping fault segments can become destructive as a result of dynamic weakening. Nature, 493(7433), pp.518-521.Okada, Y. (1985), Surface deformation due to shear and tensile faults in a half-space, *Bulletin of the Seismological Society of America*, *75*(4), 1135-1154.Okazaki, K., and G. Hirth (2016), Dehydration of lawsonite could directly trigger earthquakes in subducting oceanic crust, *Nature*, *530*(7588), 81-84.Peyrat, S., et al. (2006), Tarapacá intermediate-depth earthquake (Mw 7.7, 2005, northern Chile): A slab-pull event with horizontal fault plane constrained from seismologic and geodetic observations, *Geophys Res Lett*, *33*(22), doi:10.1029/2006gl027710.Prieto, G. A., G. C. Beroza, S. A. Barrett, G. A. López, and M. Florez (2012), Earthquake nests as natural laboratories for the study of intermediate-depth earthquake mechanics, *Tectonophysics*, *570*, 42-56.Prieto, G. A., M. Florez, S. A. Barrett, G. C. Beroza, and E. Poveda (2013), Seismic evidence for thermal runaway during intermediate-depth earthquake rupture, *Geophys Res Lett*, *40*.Ranero, C. R., J. P. Morgan, K. D. Mcintosh, and C. Reichert (2003), Bending-related faulting and mantle serpentinization at the Middle America trench, *Nature*, *425*(6956), 367-373.Sandiford, D., L. Moresi, M. Sandiford, and T. Yang (2019), Geometric controls on flat slab seismicity, *Earth Planet Sc Lett*, *527*, 115787, doi:10.1016/j.epsl.2019.115787.Scripps Institution of Oceanography. (1986). Global Seismograph Network - IRIS/IDA [Data set]. International Federation of Digital Seismograph Networks. https://doi.org/10.7914/SN/IIShi, Q., S. Wei, and M. Chen (2018), An MCMC multiple point sources inversion scheme and its application to the 2016 KumamotoMw 6.2 earthquake, *Geophysical Journal International*, *215*(2), 737-752.Sibson, R.H., (1973). Interactions between temperature and pore-fluid pressure during earthquake faulting and a mechanism for partial or total stress relief. *Nature Physical Science*, 243(126), pp.66-68.Rice, J.R., (2006). Heating and weakening of faults during earthquake slip. *Journal of Geophysical Research: Solid Earth*, 111(B5), doi:10.1029/2005JB004006.Tanikawa, W. and Shimamoto, T., 2009. Frictional and transport properties of the Chelungpu fault from shallow borehole data and their correlation with seismic behavior during the 1999 Chi-Chi earthquake. Journal of *Geophysical Research: Solid Earth*, 114(B1).Viesca, R. C., and D. I. Garagash (2015), Ubiquitous weakening of faults due to thermal pressurization, *Nature Geoscience*, *8*(11), 875-879, doi:10.1038/ngeo2554.Wang, R., B. Schurr, C. Milkereit, Z. Shao, and M. Jin (2011), An Improved Automatic Scheme for Empirical Baseline Correction of Digital Strong-Motion

Records, *Bulletin of the Seismological Society of America*, *101*(5), 2029-2044, doi:10.1785/0120110039.Wang, T., S. Wei, X. Shi, Q. Qiu, L. Li, D. Peng, R. J. Weldon, and S. Barbot (2018), The 2016 Kaikōura earthquake: Simultaneous rupture of the subduction interface and overlying faults, *Earth & Planetary Science Letters*, *482*, 44-51.Warren, L.M., (2014). Dominant fault plane orientations of intermediate-depth earthquakes beneath South America. *Journal of Geophysical Research: Solid Earth*, 119(7), pp.5762-5785.Wei, S., J. P. Avouac, K. W. Hudnut, A. Donnellan, J. W. Parker, R. W. Graves, D. Helmberger, E. Fielding, Z. Liu, and F. Cappa (2015), The 2012 Brawley swarm triggered by injection-induced aseismic slip, *Earth & Planetary Science Letters*, *422*(Complete), 115-125.Wei, S., M. Chen, X. Wang, R. W. Graves, E. O. Lindsey, T. Wang, C. Karakas, and D. V. Helmberger (2018), The 2015 Gorkha (Nepal) earthquake sequence: I. Source modeling and deterministic 3D ground shaking, *Tectonophysics*, *722*, 447-461.Wei, S., et al. (2011), Superficial simplicity of the 2010 El Mayor–Cucapah earthquake of Baja California in Mexico, *Nature Geoscience*, *4*(9), 615-618, doi:10.1038/ngeo1213.Wei, S., R. W. Graves, D. V. Helmberger, J. Avouac, and J. Jiang (2012), Sources of shaking and flooding during the Tohoku-Oki earthquake: A mixture of rupture styles, *Earth Planet Sc Lett*, *333*, 91-100.Wei, S., D. V. Helmberger, Z. Zhan, and R. W. Graves (2013), Rupture complexity of the Mw 8.3 sea of okhotsk earthquake: Rapid triggering of complementary earthquakes?, *Geophys Res Lett*, *40*(19), 5034-5039.Wibberley, C. A. J., and T. Shimamoto (2005), Earthquake slip weakening and asperities explained by thermal pressurization, *Nature*, *436*(7051), 689-692, doi:10.1038/nature03901.Yague-Martinez, N., P. Prats-Iraola, F. Rodriguez Gonzalez, R. Brcic, R. Shau, D. Geudtner, M. Eineder, and R. Bamler (2016), Interferometric Processing of Sentinel-1 TOPS Data, *IEEE Transactions on Geoscience and Remote Sensing*, *54*(4), 2220-2234, doi:10.1109/tgrs.2015.2497902.Ye, L., T. Lay, and H. Kanamori (2020), Anomalously low aftershock productivity of the 2019 MW 8.0 energetic intermediate-depth faulting beneath Peru, *Earth Planet Sc Lett*, *549*, 116528, doi:.Zeng, H., and S. Wei (2019), The effects of basin and lithospheric scale velocity structure and a ray-based travel time correction for the back-projection method, *AGUFM*, *2019*, S53F-0537.Zhao, L., and D. V. Helmberger (1994), Source Estimation from Broadband Regional Seismograms, *Bulletin of the Seismological Society of America*, *84*(1), 91-104.Zhu, L., and D. V. Helmberger (1996), Advancement in source estimation techniques using broadband regional seismograms, *Bulletin of the Seismological Society of America*, *86*(5), 1634-1641.Zhu, L., and L. Rivera (2002), A note on the dynamic and static displacements from a point source in multilayered media, *Geophysical Journal International*, *148*(3), 619-627.